Consistency and errors in Smoothed Particle Hydrodynamics using several approaches in a 2D pipe

E. Plaza[a,*], E. Santacruz[b,d], D. Aguila[b], R. Cobos[c], W. Angulo[g], L. Di G Sigalotti[e], and J. Klapp[f]
[a] *Centro de Nanotecnología, Instituto Venezolano de Investigaciones Científicas, Altos de pipe, Venezuela.*
[*] *Centro de Nanotecología, IVIC, Altos de Pipe, Estado Miranda, Venezuela.*
e-mail: ericvpp@gmail.com
[b] *Facultad de Ciencias Naturales y Matemáticas,*
ESPOL Polytechnic University, Guayaquil, Ecuador.
[c] *Department of Chemical Engineering, Carnegie Mellon University, Pittsburgh, USA.*
[d] *Laboratorio de Bioreología y Microfluídica,*
Pontificia Universidad Católica de Valparaíso, Valparaiso, Chile.
[e] *Departamento de Ciencias Básicas, Universidad Autónoma Metropolitana-Azcapotzalco,*
Ciudad de México, México.
[f] *Instituto Nacional de Investigaciones Nucleares, Ocoyoacac, México.*
[g] *Facultad de Ciencias Exactas y Naturales, Escuela de Ciencias Matemáticas y Físicas,*
Pontificia Universidad Católica del Ecuador (PUCE), Quito, Ecuador.

Received 10 July 2024; accepted 30 October 2024

Smoothed Particle Hydrodynamics (SPH) has become a promising tool for the simulation of fluids. Although too much research has been addressed to improve the method over the years, a comparison of the errors and consistency evolution when trying different approaches are still necessary to define the best scheme for practical applications. Here, a two-dimensional Poiseuille flow test benchmark is employed to enforce comparisons when varying the kernel, the definition of the sound speed in the pressure term, the viscosity and the Reynolds number.

Keywords: Smoothed Particle Hydrodynamics; consistency; error measures.

DOI: https://doi.org/10.31349/RevMexFis.71.020602

1. Introduction

Smoothed Particle Hydrodynamics (SPH) is a fully Lagrangian particle method originally introduced by Lucy [1] and Gingold and Monaghan [2] to deal with astrophysical flows. Since then, the method has spread into numerous applications in the areas of computational physics and engineering due to its ease of implementation, flexibility, and robustness. The Lagrangian nature of SPH enables the simulation of complex systems, such as breaking waves, splashing fluids, flow in porous media and other phenomena involving moving boundaries or interfaces, that would otherwise be very difficult to simulate using traditional grid-based schemes [3,4].

The SPH discretization is performed by means of an interpolation function commonly referred to as the kernel, using the influence of the surrounding particles to evaluate the properties of an observation point (or particle). The kernel function is made to depend on the distance between the observation particle and its neighbors as well as on the size of the kernel support defined by the smoothing length h. As for any other method, the error carried by the SPH approximation is defined by the distance between the discretized equations and the exact differential equations. This error comes from the spatial discretization when passing from the continuous to the discrete space. A second source of error comes from the implementation of the method itself in practical problems, where truncation of the kernel due to the presence of physical boundaries, particle disorder, and spatially and temporally varying smoothing lengths are some of the causes that give rise to a loss of consistency and therefore poor convergence. A numerical drawback of SPH is the absence of particle consistency, which affects the accuracy and convergence of the method.

Consistency refers to how well a numerical method approximates the actual differential or integral equation as the step size approaches zero. It measures the error introduced in a single step of the numerical method. A numerical method is said to be consistent if the local truncation error (the error made in one step) tends to zero as the step size tends to zero. Convergence, on the other hand, refers to the behavior of the numerical solution as the step size decreases. A numerical method is said to be convergent if the solution produced by the method approaches the exact solution of the differential or integral equation as the step size goes to zero [5,6].

In SPH the convergence has been explored in the limit when $h \rightarrow 0$ the kernel function tends to the Dirac-δ distribution, and the exact solution of the differential equations follows [2]. In the discrete case, however, where h is finite, Rasio [7] showed that the convergence properties of SPH are also a function of both the total number of particles N and the number of neighbors n within the kernel support. The SPH simulations of Gabbasov *et al.* [8] and Read *et al.* [9] showed that consistency is completely lost due to zeroth-order error terms, which would persist when working with a finite number of neighbors even though $N \to \infty$ and $h \to 0$. Zhu *et al.* [10] demonstrated that full particle consistency can be restored only in the joint limit $N \to \infty$, $h \to 0$, and $n \to \infty$, providing good evidence that the SPH discretization error is not only related to the finite number of particles filling the computational domain, but also to the size of h and the number of neighbors filling the kernel support. A numerical error analysis reported by Sigalotti *et al.* [11] have confirmed Zhu *et al.*, findings. The formal demonstration of the dependence of the SPH truncation errors on the interpolation parameters h, N, and n have been recently reported by Sigalotti *et al.* [12]. On the other hand, Violeau and Fonty [13] have computed the exact SPH error as a function of the kernel standard deviation using a differential operator applied to the interpolated field.

Many applications in the fields of mechanical, chemical, and petroleum engineering involve slow as well as fast viscous incompressible flows in pipes and conduits. An exact solution to the case of viscous fluids in pipes can be found in the classical literature [14]. This solution can be used as a benchmark test to evaluate the errors carried by the numerical solution. Since errors in practical SPH simulations can also depend on several other factors, such as the type of kernel function, the truncation of the kernel near physical boundaries, the pressure through the equation of state, the form of the viscosity and also on definition of sound speed c_s which is related with convergence and the Courant condition for weakly compressible approach, here we explore the influence of these factors on the simulation of pipe flow. On the other hand, studies of SPH consistency have been reported for the simulation of astrophysical flows [8] and anisotropic dispersion of contaminants [15]. However, as far as we know, such analyses have not been performed to the case of flow in pipes.

In this paper we report numerical experiments to evaluate the error and SPH consistency in simulations of pipe flow. The performance of the method is first explored by evaluating the influence of the kernel function on the solution. Since in most practical applications incompressible fluids are usually involved, it is a common practice in SPH to model such fluids using a weakly compressible approach through the use of a polytropic-like equation of state [16], in which case the pressure is made to depend explicitly only on the local density. Therefore, the particle motion is driven by local density gradients. In order to keep density fluctuations at a low level the sound speed is artificially imposed. Several criteria exist in the literature to define the sound speed [17-20] and therefore, it is worth exploring how this factor may influence the numerical solution.

In a Lagrangian fluid, the viscous forces over a particle are exerted by its surrounding companions. This can be an important issue in the vicinity of a boundary since the fluid-solid interaction is not embodied by the equation of motion. In general, the SPH treatment of viscosity in a rigorous manner is difficult because it is necessary to find a stable and accurate SPH representation for the second-order spatial derivatives of the velocity. In this context, a popular approach in the SPH community has been to use an artificial viscosity, which is equivalent to a bulk viscosity but acting effectively on an irregular motion on the short scale [21], and the so-called laminar viscosity proposed by Lo and Shao [22]. In general, the artificial viscosity is used to mediate strong discontinuities in shock problems with large Reynolds numbers (Re), while the laminar viscosity is suitable for low Re.

When the average velocity increases, the total error also increases, because one or more particles can achieve a large velocity compared to their immediate neighbors, thereby affecting the solution. On the other hand, the viscosity may also affect the solution when the particles are disordered, in which case the averaging of the momentum term is not homogeneous, causing small errors that may increase during the evolution.

In order to understand how these issues may affect error, consistency, and consequently convergence in the SPH simulation of pipe flows, we consider numerical calculations of time-dependent plane Poiseuille flow at different Reynolds regimes using different approaches. In the present numerical experiments a measurement of how the different approaches may affect the overall convergence is studied in the case when: (i) two different kernels (a Gaussian kernel and a Wendland function) are used for two different Reynolds regimes, (ii) the value of the artificial sound speed in the equation of state is varied for three different Reynolds regimes, and (iii) the artificial versus laminar viscosity are used. The plan of the paper is as follows: The SPH method employed and the details of the pipe flow model calculation are briefly described in Sec. 2. The consistency relations aimed at measuring the quality of the SPH convergence are given in Sec. 3. Section 4 present the results of the numerical simulations and Sec. 5 contains the conclusions.

2. Numerical scheme and pipe flow model

2.1. The SPH method

SPH is a particle-based, Lagrangian computational method used for simulating the mechanics of continuous media. The method reconstructs a continuous field at any point in space and time from a cloud of discrete particles which are the property carriers. This is accomplished by employing a three-dimensional (3D) interpolation of the scattered data using the following approximation [2,23]

$$\langle f(\mathbf{r})\rangle = \int_V f(\mathbf{r}')W(\mathbf{r}-\mathbf{r}',h)d\mathbf{r}' + O(h^2), \qquad (1)$$

where $f(\mathbf{r})$ is any scalar function defined over a volume V, $W(\mathbf{r}-\mathbf{r}',h)$ is the interpolation kernel, h is its characteristic width (known as the smoothing length), and $d\mathbf{r}'$ is a differential volume element. The function $\langle f(\mathbf{r})\rangle$ is commonly referred to as the kernel approximation of the exact function $f(\mathbf{r})$. This expression comes from the well-known sampling property of the Dirac-δ distribution by simply replacing the Dirac-δ distribution by the interpolation kernel. The second-order accuracy of the kernel approximation arises from the vanishing of the kernel gradient at $\mathbf{r} = \mathbf{r}'$, [24,25], for any finite density $\rho(\mathbf{r})$.

From Eq. (1), it is possible to derive the discretized form of any function f_i, in terms of the kernel W_{ij}

$$f_i = \sum_{j=1}^{N} \frac{m_j}{\rho_j} f_j W_{ij}, \tag{2}$$

where $f_i = f(\mathbf{r}_i)$ is the particle approximation of the function at the position of the observation particle i, $W_{ij} = W(\mathbf{r}_i - \mathbf{r}_j, h)$, while m_j, $\rho_j = \rho(\mathbf{r}_j)$ and $f_j = f(\mathbf{r}_j)$ denote, respectively, the values of the mass, density, and position of neighboring particle j.

Almost all modern applications of SPH assume that W has a compact support, that is, $W(\mathbf{r}-\mathbf{r}', h) = 0$ for $|\mathbf{r}-\mathbf{r}'| \geq kh$, where usually $k \leq 3$. This way the total number of particles N in the summation (3) is replaced by the number n of nearest neighbors of particle i within the kernel support. Equation (2) represents the basis of all SPH formulations. For the SPH discretization of a field, it would be necessary to have a suitable approximation for the spatial derivatives of any given quantity. In SPH, a number of estimators can be constructed for the gradient of a scalar field. For instance, a commonly used estimator has the pairwise symmetric form:

$$(\nabla f)_i = \rho_i \sum_{j=1}^{n} m_j \left(\frac{f_i}{\rho_i^2} + \frac{f_j}{\rho_j^2} \right) \nabla_i W_{ij}. \tag{3}$$

However, this representation is not exact for a constant function. It is particularly convenient for approximating the pressure gradient $(\nabla p)/\rho$ in the Navier-Stokes equations because it improves the angular momentum conservation [19]. This is also the form of the gradient that arises naturally from a Lagrangian formulation of the fluid equations.

Although SPH has been successfully applied to a wide range of problems in science and engineering [18,23,26-29,30,31] there are still pending issues to solve associated with its convergence. A longstanding problem has been the loss of consistency due to the kernel truncation at and near physical boundaries as well as particle disorder and the use of spatially and varying smoothing lengths. The inconsistency persists even when the join limit $N \to \infty$ and $h \to 0$ is achieved with a finite number of neighbors within the kernel support. The inconsistency arises because of zeroth-order errors are inherent in the SPH discretization [9]. The errors carried by the SPH approximation (2) encompass both the $O(h^2)$ errors carried by the kernel approximation and those carried by the particle discretization, which is due to incomplete sampling of the smoothing kernel. These errors come into evidence when using the above approximations for a constant function, $f(\mathbf{r}) = 1$, and its gradient, $\nabla f(\mathbf{r}) = 0$, *i.e.*,

$$\sum_{j=1}^{n} \frac{m_j}{\rho_j} W_{ij} \neq 1, \tag{4}$$

and

$$\frac{1}{\rho_i} \sum_{j=1}^{n} m_j \left(1 + \frac{\rho_i^2}{\rho_j^2} \right) \nabla_i W_{ij} \neq 0. \tag{5}$$

The errors associated with the kernel approximation are minimized by reducing the smoothing length, while the zeroth-order errors carried by the particle approximation are reduced by increasing the number of neighbors within the kernel support [10,8]. A fully consistent scheme is therefore obtained in the joint limit $h \to 0$ and $n \to \infty$, when the total number of particles filling the computational domain also tends to infinity. In this limit, the zeroth-order sampling errors vanish, and the particle discretization error tends to the second-order kernel approximation. This means that in this limit, the particle approximations for the constant function and zero gradients in Eqs. (4) and (5) will tend to one and zero, respectively. Thus, for a finite number of particles, the most accurate SPH scheme results from working with large numbers of neighbors and small smoothing lengths [11]. However, this makes the simulations expensive from the computational point of view, thereby requiring efficiency improvements [32]. While these two requirements seem most important for simulating compressible fluids, other problems within the method itself and the implementation of mathematical improvements require attention. Here, we test how the kernel function, pressure value, and viscosity formulation can affect the error, and consistency properties of SPH for weakly compressible flows; in applications of SPH to incompressible fluids, the equation to be discretized is the Navier-Stokes equation for the temporal rate of change of fluid velocity.

$$\frac{d\mathbf{v}}{dt} = -\frac{1}{\rho} \nabla p + \frac{\eta}{\rho} \nabla^2 \mathbf{v} + \mathbf{g}, \tag{6}$$

where η is the dynamic viscosity, **v** the velocity, and **g** the gravity

Moreover, in SPH there are two traditional forms to account for viscous dissipation. The first form is given by the so-called artificial viscosity introduced by Monaghan [24] and the second one, which is mostly used in applications to pipe flow, is the laminar viscosity of Lo and Shao [22]. The SPH approximation of Eq. (6) with the viscous term represented by the laminar viscosity is given by [22]

$$\begin{aligned} \frac{d\mathbf{v}_i}{dt} &= \sum_{j=1}^{N} m_j \left(\frac{p_i}{\rho_i^2} + \frac{p_j}{\rho_j^2} \right) \nabla_i W_{ij} \\ &\quad + 4\nu \sum_{j=1}^{N} m_j \frac{\mathbf{v}_i - \mathbf{v}_j}{\rho_i + \rho_j} \frac{\mathbf{r}_{ij} \cdot \nabla_i W_{ij}}{|\mathbf{r}_{ij}|^2 + \epsilon^2}. \end{aligned} \tag{7}$$

Here, the term $\mathbf{v}$ refers to the velocity of the particles, $\mathbf{r}$ to their position, and the term ϵ is a factor that prevents the right-hand side of the equation from becoming infinite, which, for the purposes of this work, was defined as $\epsilon = 0.001$.

To close the system of discrete equations it is necessary to define a pressure-density relation, which for weakly compressible flows is given by the relation [16]

$$p = p_0 \left[\left(\frac{\rho}{\rho_0} \right)^{\gamma} - 1 \right], \tag{8}$$

where $\gamma = 7$, $p_0 = c_0^2 \rho_0/\gamma$, ρ_0 is a reference density, for this work, it was defined as that of water at ambient temperature, and c_0 is the speed of sound in the medium. Setting $f \to \rho$ in the summation interpolant (3), the following equation is the alternative SPH form of the mass conservation equation.

$$\rho_i = \sum_{j=1}^{n} m_j W_{ij}. \tag{9}$$

The fluid acceleration in Eq. (7) can be evaluated once the pressure and density are calculated according to Eqs. (8) and (9), respectively. A direct evaluation of second-order derivates is not required, and the Wendland function (10) will be used as the interpolation kernel [33,34]:

$$W(q,h) = \frac{7}{4\pi h^2} \left(1 - \frac{q}{2}\right)^4 (2q+1), \tag{10}$$

were $q = \text{—}\mathbf{r}\text{—}_{ij}/h$ if $|\mathbf{r} - \mathbf{r}'| \leq h$ and 0 otherwise.

2.2. Poiseuille flow model

For time-dependent Poiseuille flow in a plane, the Navier-Stokes equation (6) admits the analytical solution

$$\begin{aligned} v_x(y,t) = {} & \frac{F}{2\nu}\left(y^2 - d^2\right) + \sum_{k=0}^{\infty} \frac{16(-1)^k d^2 F}{\nu \pi^3 (2k+1)^3} \\ & \times \cos\left(\frac{(2k+1)\pi y}{2d}\right) \\ & \times \exp\left(\frac{-(2k+1)^2 \pi^2 \nu t}{4d^2}\right), \end{aligned} \tag{11}$$

where d is half distance between the parallel plates of the channel and the $\nu = \eta/\rho$ is the kinematic viscosity. The fluid is moved by applying a force proportional to the pressure difference Δp, which is equal to $F = -2\nu v_0/d^2$ in terms of the flow velocity v_0 at the center of the pipe.

This solution is valid for laminar flows. In our case, it will be employed to compare against numerical results for Reynolds numbers below or equal to 100, ensuring we remain within the laminar flow regime [35]. For the purposes of this work, all codes were executed using Matlab on an i7 computer with 16GB of RAM. A Verlet integration scheme was employed for all the simulations.

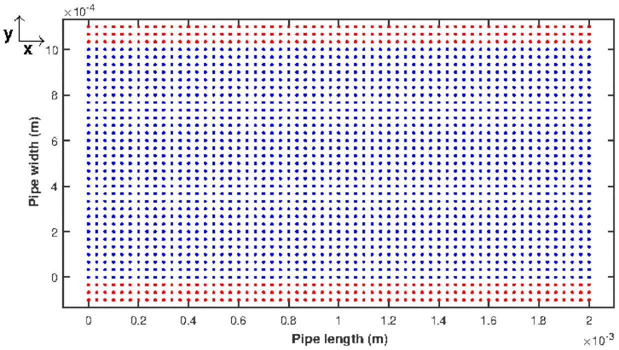

FIGURE 1. Schematic drawing showing the initial particle distribution. The blue particles represent the fluid domain, while the red ones are ghost particles.

A reference calculation of Poiseuille flow using the scheme of previous section is presented for a density $\rho = 1000$ kgm^{-3}, a pipe diameter $d = 0.001$ m, and pipe length of twice its width, *i.e.*, $L = 0.002$ m. The inter-particle spacing was set to $ds = 3.3 \times 10^{-5}$ m and the smoothing length to $h = 1.8ds = 6 \times 10^{-5}$ m. Equation (8) was used as the pressure density relation with $\gamma = 7$ as it is suitable for water. Steady flow is achieved after 6000 time steps, using a time stepping of $\delta t = 0.0001$ s, which amounts to 0.6 s. A total number of $N = 1891$ initially uniformly distributed particles is used to represent the fluid and the boundaries were modeled using 360 ghost particles as shown in Fig. 1. This amounts to three rows of particles above the upper plate and below the lower plate.

In order to limit the relative density fluctuations to approximately 1% and mimic a weakly compressible fluid, a sound speed large enough to control density fluctuations but small enough to avoid a stiff stability restriction on the time step is imposed. This approach has been also used in grid-based methods to model incompressible fluids [36]. For the present test the speed of sound was defined to be $c_0 = 0.1 v_{\max}$, where $v_{\max}$ is the estimated maximum velocity defined as a function of Re, *i.e.*, $v_{\max} = Re\eta/L = 2.51 \times 10^{-5}$ ms^{-1} for this particular case. Therefore, c_0 is made to depend upon the initial velocity [18]. In this particular case a Reynolds regime of 0.025 was set. Inlet-outlet boundary conditions appropriate for laminar flow were imposed at the entrance and exit of the pipe, following the method outlined in Alvarado's work [37]. At the pipe outlet, there is a region outside the computational domain that allows for the calculation of the kernel to reduce the truncation effect of the kernel at the pipe exit and the associated error.

The left panel of Fig. 2 shows the numerically obtained velocity profiles at three different times (symbols) as compared with the analytical solution (solid line) as given by Eq. (11). The right panel shows the corresponding percent error between the numerical and analytical solution.

The error varies from a maximum value of $\approx 6.25\%$ close to the pipe boundaries to a minimum value of about 0.08% in the center of the pipe, where the flow is fully developed. In order to gain insight into the convergence and therefore the particle consistency for this model calculation, we shall explore the effects of changing several conditions. Although

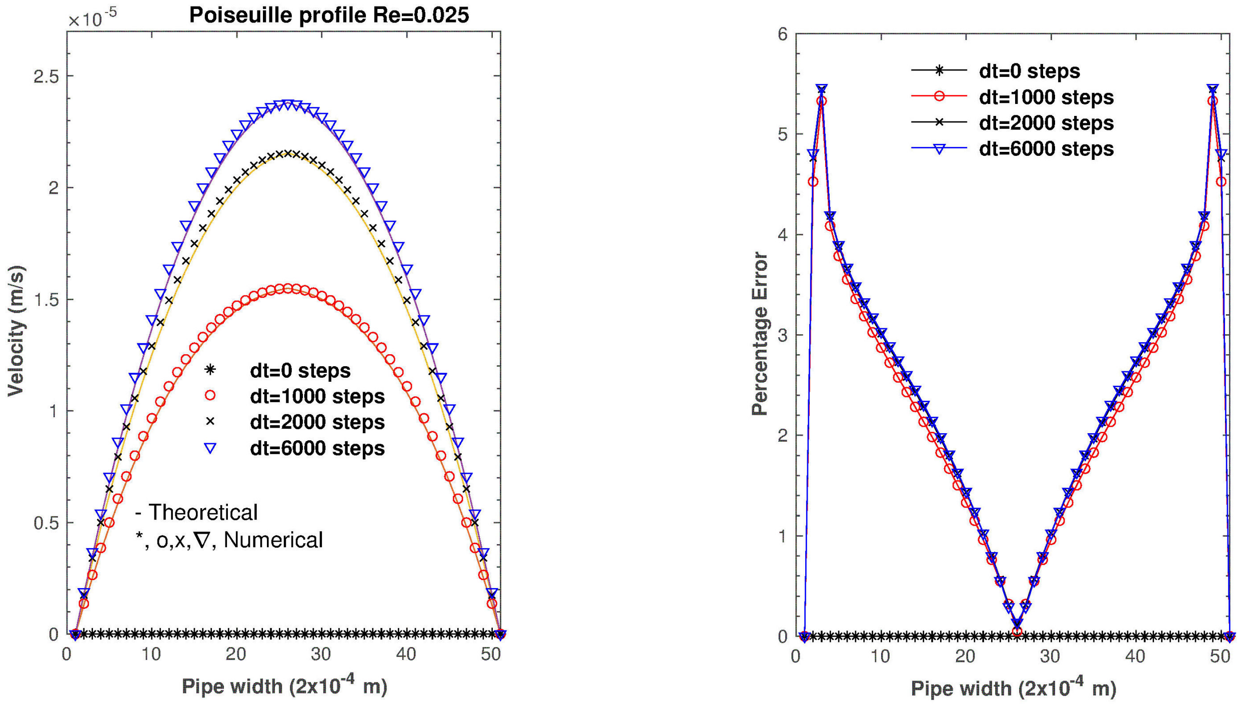

FIGURE 2. a) Numerically obtained Poiseuille velocity profile at three different times until steady-state is achieved after 0.6 s (symbols) as compared with the analytical solution (solid line). b) Percent error between the numerical and analytical solutions for the same times displayed in the left panel.

the test model under consideration is a very simple one, the improvements are applicable to more complex flows and pipe geometries.

3. Particle consistency relations

Estimation of the error carried by a numerical simulation requires comparing the exact solution with the numerical one. Although it is possible to measure this error theoretically [11-13], comparing the exact and numerical solutions may be useful to estimate the influence of other aspects involved in the numerical solution. In particular, the consistency is related to how closely the exact equations are approximated by the discrete equations. Therefore, consistency is a measure of the local truncation error. This work is concerned with testing the influence of different approaches on the local truncation error carried by the numerical solution. One way to check whether a numerical solution is converging to the exact solution is by monitoring during the evolution the behavior of the so-called SPH consistency relations, which can be derived by means of Taylor series expansions [8,11]. In order to see if C^1-consistency (or second-order accuracy) is achieved, it suffices to calculate the temporal evolution of the zeroth- and first-order moments of the kernel and its gradient, which in discrete form read as follows

$$\mathbf{M}_{0,a} = \sum_{b=1}^{n} W_{ab}\Delta V_b, \tag{12}$$

$$\mathbf{M}_{1,a} = \sum_{b=1}^{n} \mathbf{r}_{ba} W_{ab}\Delta V_b, \tag{13}$$

$$\mathbf{M}'_{0,a} = \sum_{b=1}^{n} \nabla_a W_{ab}\Delta V_b, \tag{14}$$

$$\mathbf{M}'_{1,a} = \sum_{b=1}^{n} \mathbf{r}_{ba} \nabla_a W_{ab}\Delta V_b, \tag{15}$$

where $\mathbf{r}_{ba} = \mathbf{r}_b - \mathbf{r}_a$, $\Delta V_b = m_b/\rho_b$ is the volume of particle b, m_b is its mass, and ρ_b is its density. Equation (12) is the normalization condition (or zeroth-order moment) of the kernel, while Eq. (13) is the first-order moment of the kernel. Equations (14) and (15) are, respectively, the zeroth- and first-order moments of the kernel gradient. C^0-particle consistency of the kernel demands that $M_{0,a} = 1$, while C^1-particle consistency is always guaranteed because $\mathbf{M}_{1,a} = \mathbf{0}$ owing to the symmetry of the kernel, where $\mathbf{0} = (0,0,0)$ is the null vector. On the other hand, C^0-particle consistency for the gradient estimate requires that $\mathrm{M}'_{0,a} = \mathbf{0}$, while C^1-particle consistency is achieved when $\mathrm{M}'_{1,a} = \mathbb{1}$, where $\mathbb{1}$ is the identity tensor. These quantities measure the quality of particle consistency during the evolution for most practical SPH applications. This approach was first tested in SPH simulations of astrophysical flows in the absence of physical boundaries [8].

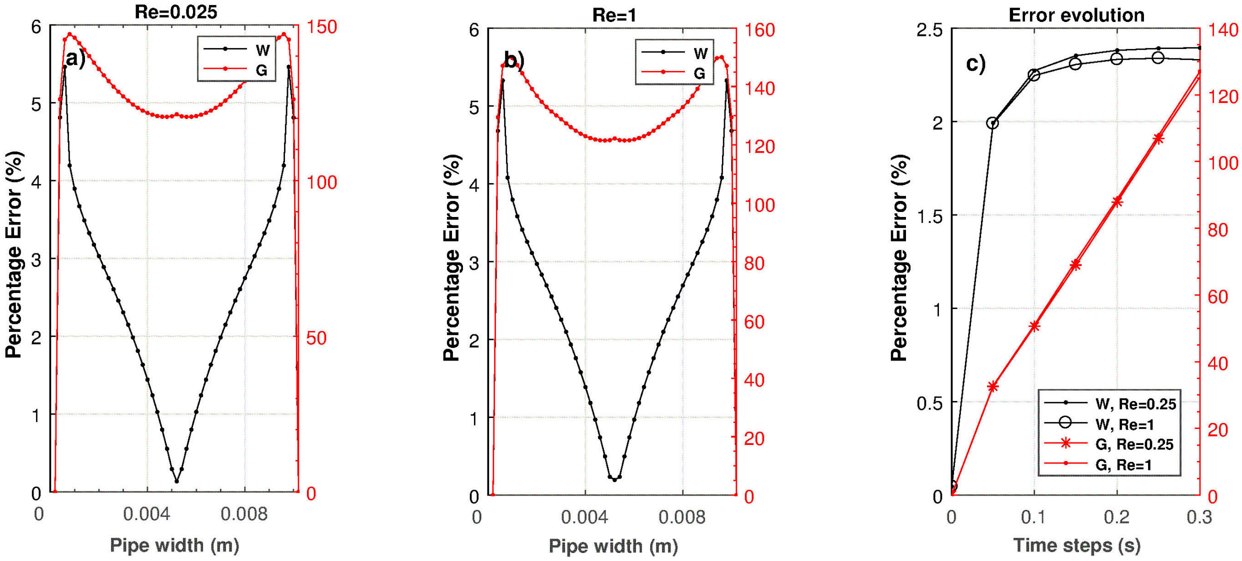

FIGURE 3. Percent error and error evolution as a function of time for Poiseuille flow at 0.3 s for Re $= 0.025$ a) and 1.0 b). The red and black curves correspond to the model simulation with the Gaussian kernel and the Wendland function, respectively. Figure c) depicts the time evolution of the root-mean-square error (RMSE) for the same calculations of Figs. a) and b).

4. Numerical results

4.1. The kernel function

In SPH the properties of an observation particle are determined from the properties of its neighbors by means of the interpolating kernel. The influence of the kernel on the overall error of the numerical solution is here explored by comparing the performance of the consistency relations when using the Gaussian kernel

$$W(\mathbf{r}-\mathbf{r}',h)=\alpha\exp\left(\frac{-|\mathbf{r}-\mathbf{r}'|}{h}\right)^2, \qquad (16)$$

where $\alpha = 1/(\pi h^2)$ in two dimensions, and the Wendland function, defined previously in Eq. (10) [33,34].

In particular, Wendland functions have become quite popular because of its ability to support a large number of neighbors without suffering from tensile instabilities, which occur when particles are in a state of tensile stress, causing their motion to become unstable. This can lead to particle clumping or even a complete blowup in the computation [23].

On the other hand, the choice of the Gaussian kernel is due to the fact that it is known to be stable and sufficiently smooth even for higher order derivatives.

Two model calculations with Re $= 0.025$ and 1.0 were employed for the present numerical experiments, starting with a fluid density $\rho = 1000$ kgm^{-3}, as is adequate for water at ambient temperature. The pipe diameter was set to $d = 0.001$ m and its total length to $L = 0.002$ m. The fluid domain was filled with, 11000 uniformly distributed particles with spacing $ds = 2\times10^{-5}$ m along the x- and y-directions, while a total number of 1500 ghost particles were used to model the pipe wall boundaries. The value of the smoothing length was chosen to be $h = 1.8ds = 3.6\times10^{-5}$ m. The evolution was calculated with a time stepping $\delta t = 5\times10^{-5}$ s and the errors were measured after 6000 time steps (*i.e.*, after 0.3 s) when the flow reached steady-state conditions. As in the reference calculation of Fig. 1, the sound speed was set to $c_0 = 0.1v_{\max}$, where $v_{\max}$ is the estimated maximum velocity. In this particular case, $v_{\max} = 2.51\times10^{-5}$ ms^{-1} (for Re $= 0.025$) and 0.001004 ms^{-1} (for Re $= 1.0$). Inlet and outlet boundary conditions were employed at the entrance and exit of the pipe, where particles leaving the computational domain on the right side are forced to enter on the left side at the same height and with the same velocity.

Figure 3 shows the percent errors of the steady-state solution for the velocity at 0.3 s. The results for Re $= 0.025$ and 1.0 are displayed in Figs. 3a) and b), respectively. A maximum error of $\approx 147.07\%$ occurs near the wall boundary for Re $= 0.025$ when working with the Gaussian kernel. A similar behavior is found for Re $= 1.0$ with maximum errors of about 150% close to the wall boundaries. The same calculations with the Wendland function resulted in considerably much lower errors everywhere. The lowest errors for both the Gaussian kernel and the Wendland function occur at the pipe center, where the maximum error is less than about 5.3% for both Re = 0.025 and 1.0 in the Wendland case. The maximum error for the Gaussian kernel is close to 150% at the boundaries in both cases Re $= 0.025$ and 1.0. Evidently, the Wendland function provides a superior performance compared to the Gaussian kernel. Figure 3c) depicts the time evolution of the root-mean-square error (RMSE) for all four models. There is actually little difference when increasing Re from 0.025 to 1.0 in both cases. However, the RMSEs are seen to grow almost linearly in the calculations with the Gaussian kernel, reaching values close to 130% by 0.3 s. In contrast, when working with the Wendland function, the RMSEs grow at a faster rate during the first 0.05 s when they become close

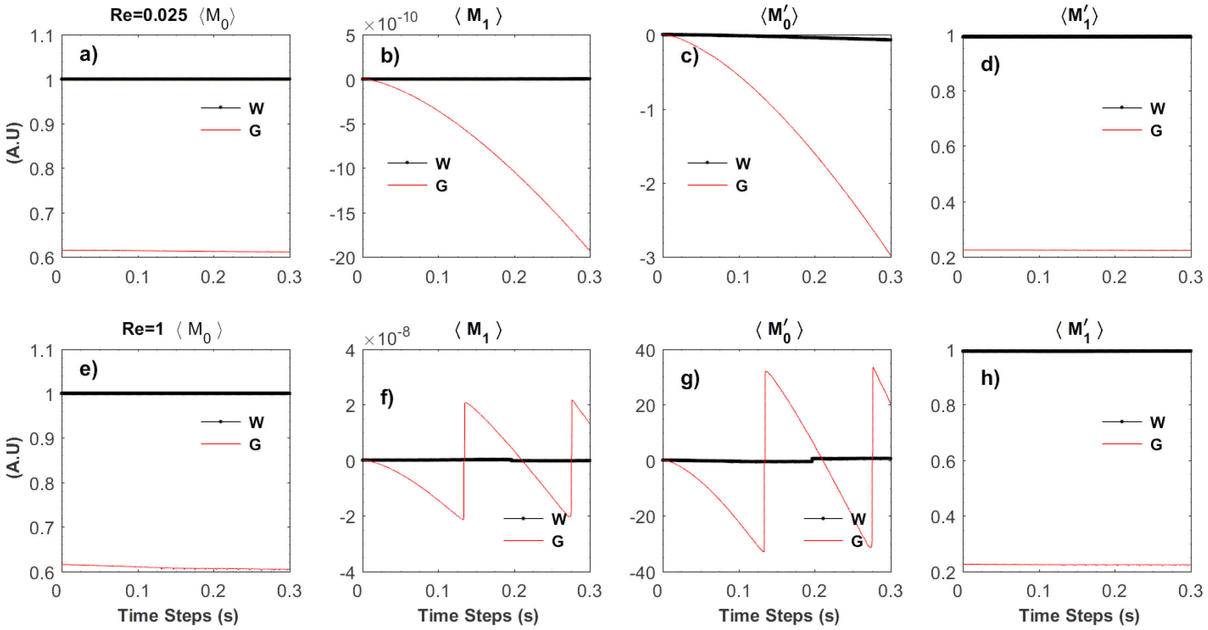

FIGURE 4. Figures a), e) and b), f) show the zeroth- and first-order moments of the kernel, respectively, while Figs. c), g) and d), h) show the zeroth- and first-order moments of the gradient, respectively, as a function of time for Poiseuille flow at 0.3 s for Re= 0.025 (top figures) and 1.0 (bottom figures). The black curves depict the moments for the simulation with the Wendland function, while the red ones do the same for the Gaussian kernel.

TABLE I. Maximum errors and maximum spread values of the zeroth- and first-order moments of the kernel and its gradient for the Gaussian and Wendland kernels for two different values of Re.

	Error Max (%)		First moments of the kernel (a.u)				First moments of the gradient (a.u)			
	Gaussian	Wendland	Gaussian		Wendland		Gaussian		Wendland	
			$\langle M_0\rangle$	$\langle \mathbf{M_1}\rangle$	$\langle M_0\rangle$	$\langle \mathbf{M_1}\rangle$	$\langle \mathbf{M'_0}\rangle$	$\langle \mathbf{M'_1}\rangle$	$\langle \mathbf{M'_0}\rangle$	$\langle \mathbf{M'_1}\rangle$
Re $= 0.025$	147.07	5.46	0.6154	-1.92×10^{-9}	1.0001	3.2×10^{-12}	-2.9763	0.2258	-0.0716	0.9917
Re $= 1$	150.05	5.32	0.6154	-2.14×10^{-8}	1.0001	2.38×10^{-10}	33.519	0.2258	0.6347	0.9921

to 2%. Thereafter, the rate decays and approaches an almost constant trend for the remainder of the evolution, reaching values slightly above 2.2% at $t = 0.3$ s.

Figure 4 displays the time evolution of the zeroth- and first-order moments of the kernel and its gradient for both the Wendland and the Gaussian interpolation functions. The upper frames in this figure depict the case when Re $= 0.025$, while the lower frames show the evolution for Re $= 1$. Equation (12) was used to compute the time evolution of M_0 depicted in Figures 4a and e. Since $\mathbf{M}_1$ and $\mathbf{M}'_0$ are vectors, the quantities $\langle\mathbf{M}_1\rangle$ and $\langle\mathbf{M}'_0\rangle$ depicted in Figs. 4b), 4f) and 4c), 4g) correspond to mean values between their x- and y-components. Similarly, $\mathbf{M}'_1$, as given by Eq. (15), is a second-rank tensor and therefore the quantity $\langle\mathbf{M}'_1\rangle$ displayed in Figs. 4d), 4h) correspond to mean values of the diagonal components of the tensor.

The calculation with the Wendland function reproduced the normalization condition of the kernel, $M_0 = 1$, during the whole evolution with very good accuracy. In contrast, the Gaussian kernel deviates substantially from unity, with $M_0 \approx 0.6$ for both values of Re. This significant departure from unity means that C^0-particle consistency of the kernel is not guaranteed when working with the Gaussian kernel. Moreover, for Re $= 0.025$ and Re$= 1$, the calculation with the Wendland function also reproduces with a good approximation the condition $\mathbf{M}_{1,a} = \mathbf{0}$, while the same is not true for the Gaussian kernel, where significant departures from zero are evident in Figs. 4b) and 4f). In particular, When the Reynolds number is raised to unity, the simulation with the Gaussian function oscillates about zero, exhibiting a sawtooth behavior. Figures 4c), 4g) and 4d), 4h) also shows that $\langle\mathbf{M}'_0\rangle \approx 0$ and $\langle\mathbf{M}'_1\rangle \approx 1$ when using the Wendland function, implying that C^0- and C^1-particle consistencies are achieved for the kernel gradient. However, the same is not true for the Gaussian kernel, where $\langle\mathbf{M}'_0\rangle$ deviates from zero and $\langle\mathbf{M}'_1\rangle \approx 0.2$ for both values of Re. From these figures it is clear that C^0- and C^1-particle consistencies are achieved for the kernel and its gradient when working with the Wendland function, while the same calculations using the Gaussian kernel suffer from a loss of consistency. This is a consequence of the much larger errors achieved by these latter calculations close to the pipe walls (see Fig. 3). For further comparison of the errors, Table I lists the maximum errors and maximum

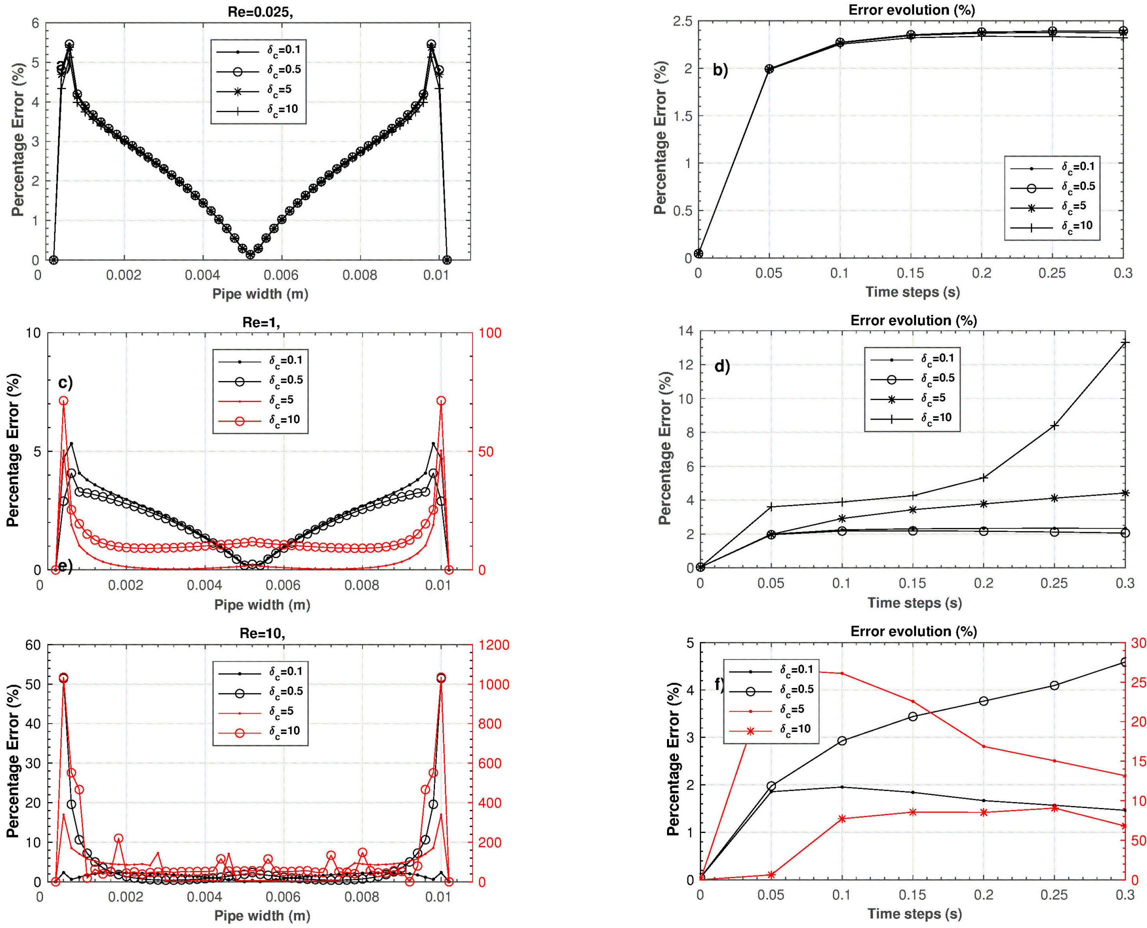

FIGURE 5. Percent error in the full section of the pipe and its time evolution up to 0.3 s when a steady-state solution is reached. The dependence of the errors on Re and the choice of δ_c is displayed in full.

values achieved by the first two moments of the kernel and its gradient for both interpolation kernels and varying Re.

4.2. The effects of pressure

Weakly compressible SPH schemes are traditionally based on the use of Eq. (8) for the calculation of the pressure [16]. However, this equation requires setting the reference value p_0, which in turn depends upon the sound speed, c_0, and the initial reference density, ρ_0. In order to keep the fluctuations in the density field at a low level, the value of c_0 is artificially set as

$$c_0 = \delta_c v_{\max}, \tag{17}$$

where δ_c is a constant parameter and $v_{\max}$ is the maximum fluid velocity. In particular, the sound speed must be large enough to control density fluctuations and avoid too small time steps. In order to keep fluctuations less than about 1% it is customary to set $\delta_c = 10$, [18]. In low Re flows, the local variations of the pressure gradient can be very small compared to the hydrostatic pressure gradient, making this approach suitable for the simulation of pipe flows [17].

In order to evaluate the effects of varying the value of δ_c on the numerical solution, the same test case model as before was employed. A total of 11000 SPH particles were used to fill the computational domain. With this choice, the initial uniform spacing between particles was $ds = 2 \times 10^{-5}$ m along the x- and y-directions, while a total number of 1500 ghost particles were used to deal with the pipe wall boundaries and the smoothing length was set equal to $h = 1.8ds = 3.6 \times 10^{-5}$ m. The effects of varying the magnitude of the pressure was tested for values of $\delta_c = 0.1$, 0.5, 5, and 10 for three different Reynolds regimes (Re $= 0.025$, 1.0, and 10). The Wendland function (18) was used as the interpolating kernel for all runs and the numerical solution was compared to the analytical one after about 0.3 s when the flow has reached a steady-state condition. Similarly to the previous case, a time stepping $\delta t = 5 \times 10^{-5}$ s was used and the errors were measured after 3000 time steps (*i.e.*, after 0.3 s). In this particular case, $v_{\max} = 2.51 \times 10^{-5}$ m s^{-1} (for Re $= 0.025$), $v_{\max} = 0.001004$ m s^{-1} for Re$= 1$, and $v_{\max} = 0.01004$ m s^{-1} for Re$= 10$.

Figure 5 shows the percent errors for all runs. The left column of frames shows the resulting percent error of the numerical solution for Re $= 0.025$, 1.0, and 10 [Figs. 4a), 4c)

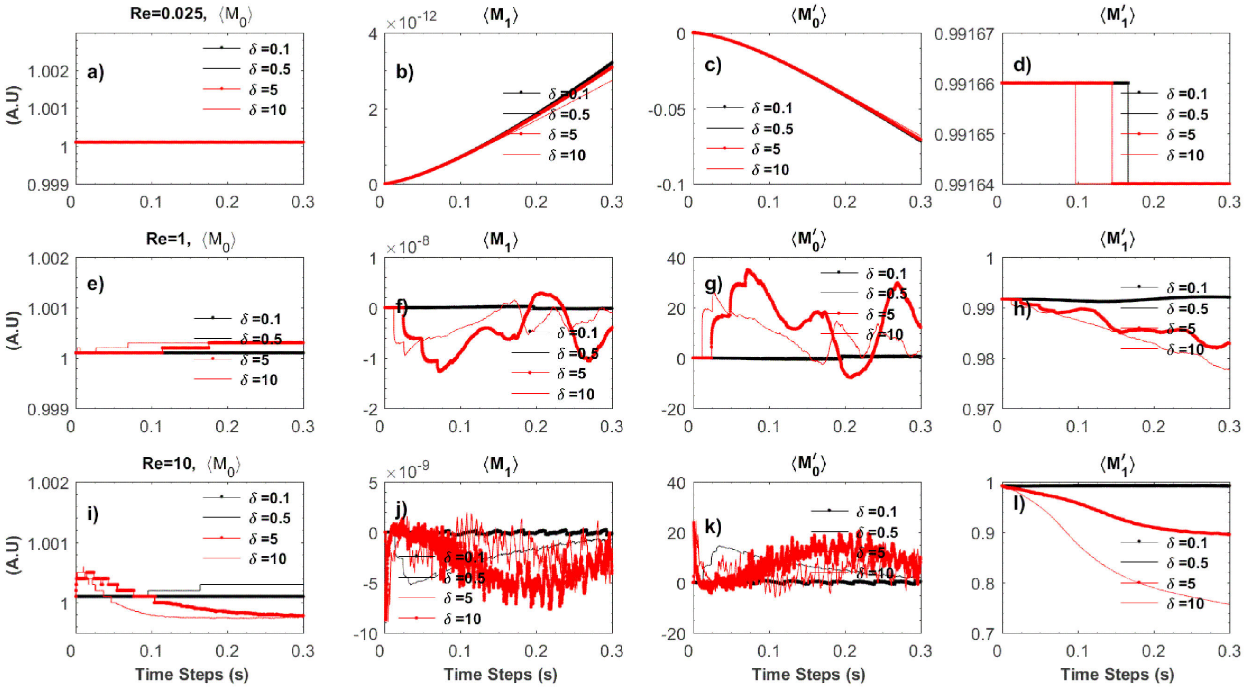

FIGURE 6. Figures a), e), i) and b), f), j) show the time evolution of the zeroth- and first-order moments of the kernel, respectively, while figures c), g), k) and d), h), i) show the same for the zeroth- and first-order moments of the gradient, respectively, for Poiseuille flow at 0.3 s for Re= 0.025 (top figures), Re= 1 (middle figures), and Re= 10 (bottom figures) and varied choices of the parameter δ_c.

and 4e)], when the values of δ_c are varied between 0.1 and 10. All curves correspond to values at the end of the simulations. For Re $= 0.025$ the error is almost independent of δ_c and grows to a maximum value of about 5% close to the pipe wall. When Re is raised to unity, the error shows a more clear dependence on δ_c. For $\delta_c \leq 0.5$, the errors behave similarly to those depicted in Fig. 5a) with maximum values between 4 and 5% near the pipe wall. When the value of δ_c is increased to 5 and 10, the errors magnify everywhere with peaks of 50 and 70% close to the pipe wall, respectively. This behavior becomes even more pronounced with peak values of about 20% for $\delta_c = 0.1$ and more than 1000% for $\delta_c = 10$ when Re $= 10$. Independently of Re, the lowest percent errors always occur when $\delta_c = 0.1$.

Figures 5b), 5d), and 5f) show the temporal evolution of the average error through the pipe section for varying δ_c and Re. When Re $= 0.025$, the error grows similarly for all values of δ_c, implying that for small Re, the choice of c_0 in the pressure equation does not affect the numerical solution. In all cases, the error grows steeply during the first 0.05 s and then slows down, reaching a value slightly below 2.5% by the end of the simulation. When Re is increased to unity, the error for $\delta_c \leq 0.5$ behaves almost in the same manner as before, and becomes larger for $\delta_c = 5$ and 10. At Re $= 10$, the errors amplify and their evolution depends more strongly on the value of δ_c. Evidently the red curves corresponding to $\delta_c = 5$ and 10 shows that the errors become exceedingly larger compared to $\delta_c = 0.1$ and 0.5. From this last figure it is clear that the errors are more sensitive to δ_c when Re is increased. As was already concluded from inspection of Figs. 4a), 4c), and 4e), the errors are kept at a relatively low level only when $\delta_c = 0.1$, regardless of the value of Re.

The time evolution of the first moments of the kernel function and its gradient are displayed in Fig. 6 for Re $=$ 0.025, 1, and 10 and varying values of δ_c between 0.1 and 10. From Figs. 6a), e), and i we may see that the normalization condition of the kernel is almost exactly recovered in the particle approximation for $\delta_c = 0.1$ [Figs. 6a)] and with a very good approximation for the other values of δ_c [Figs. 6e) and 6i)] almost independently of the Re-value. On the other hand, the first moment of the kernel keeps close to zero for Re= 0.025 regardless of the value of δ_c [Fig. 6b)], implying that C^1-consistency is approximately achieved in this case. However, when Re is raised to unity, C^1-consistency is restored only for $\delta_c \leq 0.5$, and is completely lost when $\delta_c = 5$ and 10 [see Fig. 6f)]. For Re= 10 the situation worsens as only for $\delta_c = 0.1$ is C^1-consistency restored in an approximate sense. In this case, the first moment of the kernel oscillates with very small amplitudes about zero. These small-amplitude oscillations may be the result of using periodic boundary conditions, which as Re is increased, introduce more noise into the solution in the course of the simulation.

The time evolution of the zeroth-order moment of the gradient is depicted in Figs. 6c), 6g), and 6k). The relation $\mathbf{M}'_{0,a} = 0$ is very well reproduced for Re= 0.025 almost independently of δ_c [see Fig. 6c)], implying that C^0-consistency for the gradient at this low Re-values is restored regardless of the choice of the pressure scaling. However, for Re $= 1$, C^0-consistency for the gradient is achieved only

TABLE II. Maximum percent errors and maximum spread values of the zeroth- and first-order moments of the kernel and its gradient for different δ_c values.

	δ_c	Error Max (%)	First moments of the kernel (a.u)		First moments of the gradient (a.u)	
			$\langle M_0 \rangle$	$\langle \mathbf{M_1} \rangle$	$\langle \mathbf{M_0'} \rangle$	$\langle \mathbf{M_1'} \rangle$
$\mathrm{Re} = 0.025$	$\delta_c = 0.1$	5.461	1.0001	3.20×10^{-12}	-0.0716	0.9916
	$\delta_c = 0.5$	5.460	1.0001	3.2072×10^{-12}	-0.0716	0.9916
	$\delta_c = 5$	5.377	1.0001	3.0896×10^{-12}	-0.0708	0.9916
	$\delta_c = 10$	5.127	1.0001	2.7378×10^{-12}	-0.0683	0.9916
$\mathrm{Re} = 1$	$\delta_c = 0.1$	5.327	1.0001	-2.2870×10^{-10}	0.6347	0.9912
	$\delta_c = 0.5$	4.077	1.0001	-4.5074×10^{-10}	1.2438	0.9912
	$\delta_c = 5$	50.310	1.0001	-1.2725×10^{-8}	34.986	0.9820
	$\delta_c = 10$	71.338	1.0003	-9.5240×10^{-9}	26.4480	0.9776
Re=10	$\delta_c = 0.1$	2.3178	1.0001	-3.8018×10^{-10}	-0.7557	0.9914
	$\delta_c = 0.5$	51.433	1.0003	-5.2176×10^{-9}	14.5610	0.9885
	$\delta_c = 5$	339.799	1.0005	-8.8931×10^{-9}	24.6420	0.8951
	$\delta_c = 10$	71.338	1.0006	-8.7036×10^{-9}	23.8870	0.7564

when $\delta_c \leq 0.5$ and is lost for $\delta_c = 5$ and 10 [Fig. 6g)]. When Re is increased to 10, C^0-particle consistency for the gradient is only restored for $\delta_c = 0.1$, as shown in Fig. 6k). Finally, the time evolution of the first-order moment of the gradient is displayed in Figs. 6d), 6h), and 6l). In particular, Fig. 6d) shows that the consistency relation $\mathbf{M}'_{1,a} = \mathbb{I}$ is also very well reproduced numerically for all values of δ_c when $\mathrm{Re} = 0.025$, implying C^1-particle consistency for the gradient in all cases. The same is true for $\delta_c \leq 0.5$ when Re= 1 and 10 [Figs. 6h) and 6l)].

Table II lists the maximum errors and maximum values of the first two moments of the kernel and its gradient for all models. C^1-consistency for the kernel is always restored independently of δ_c and Re. However, the same is not true for the gradient where approximate C^1-consistency is achieved only when Re= 0.025 almost independently of δ_c and only for $\delta_c = 0.1$ at larger values of Re.

4.3. Artificial versus laminar viscosity

In this section, we study how the choice of the viscous term in the momentum equation can affect convergence. In particular, we compare the results when working with an artificial and a laminar viscosity formulation. The artificial viscosity was introduced in many SPH applications to mediate strong shocks and discontinuities in the solution [19,21]. Since it has been built analogously to the real gas viscosity, it has been used in many applications to model the dynamics of viscous fluids. On the other hand, the laminar viscosity was introduced to be more in line with the definition of the viscous stress tensor [22]. This latter form is modeled by the last term on the left-hand side of Eq. (7). In contrast, the artificial viscosity, Π_{ij}, enters the momentum equation as

$$\frac{d\mathbf{v}_i}{dt} = \sum_{j=1}^{N} m_j \left(\frac{p_i}{\rho_i^2} + \frac{p_j}{\rho_j^2} + \Pi_{ij} \right) \nabla_i W_{ij} + \mathbf{g}, \tag{18}$$

where a widely used form is given by the relation

$$\Pi_{ij} = -\nu_v \left(\frac{\mathbf{v}_{ij} \cdot \mathbf{r}_{ij}}{r_{ij}^2 + \epsilon h^2} \right), \tag{19}$$

where $\epsilon = 0.01$ to prevent a singularity when the value of $\mathbf{r}_{ab}$ becomes too small, $\mathbf{v}_{ij} = (\mathbf{v}_i - \mathbf{v}_j)$, and $\mathbf{r}_{ij} = (\mathbf{r}_i - \mathbf{r}_j)$.

The proportionality factor ν_v is defined according to

$$\nu_v = \frac{\alpha_{visc} h_0 c_0}{\rho_{ab}}, \tag{20}$$

where, h_0, c_0, and α_{visc} represent the smoothing length, the sound speed, and a constant used to tune the artificial viscosity, respectively. In the numerical experiments, the value of α_{visc} was chosen to minimize the error when varying the value of the Reynolds number (Re). For example, for $\mathrm{Re} = 0.025$, the optimal value of α_{visc} was found to be 80000, while for $\mathrm{Re} = 1$, 10, 100 the optimal values of α_{visc} were found to be 2200, 200, and 25, respectively. According to this form of the artificial viscosity, when two particles approach each other they will feel a repulsive force, while when they recede from each other the force is attractive. Therefore, the viscosity term may affect the solution when too much or too low dissipation is applied to the fluid, thereby introducing an error. This is particularly important when dealing with high Reynolds numbers. In pipe flows, this is a concern because of the wall boundaries. Therefore, it is worth to compare both methods to evaluate their influence on the error carried by the numerical simulation. The same initial parameters of Sec. 4.2 were employed for the simulations. The sound speed was set by choosing $\delta_c = 0.1$ and the calculations were carried out for four different values of Re, namely $\mathrm{Re} = 0.025$, 1.0, 10, and 100. The fluid domain is filled with 11000 SPH particles and the wall boundary was implemented

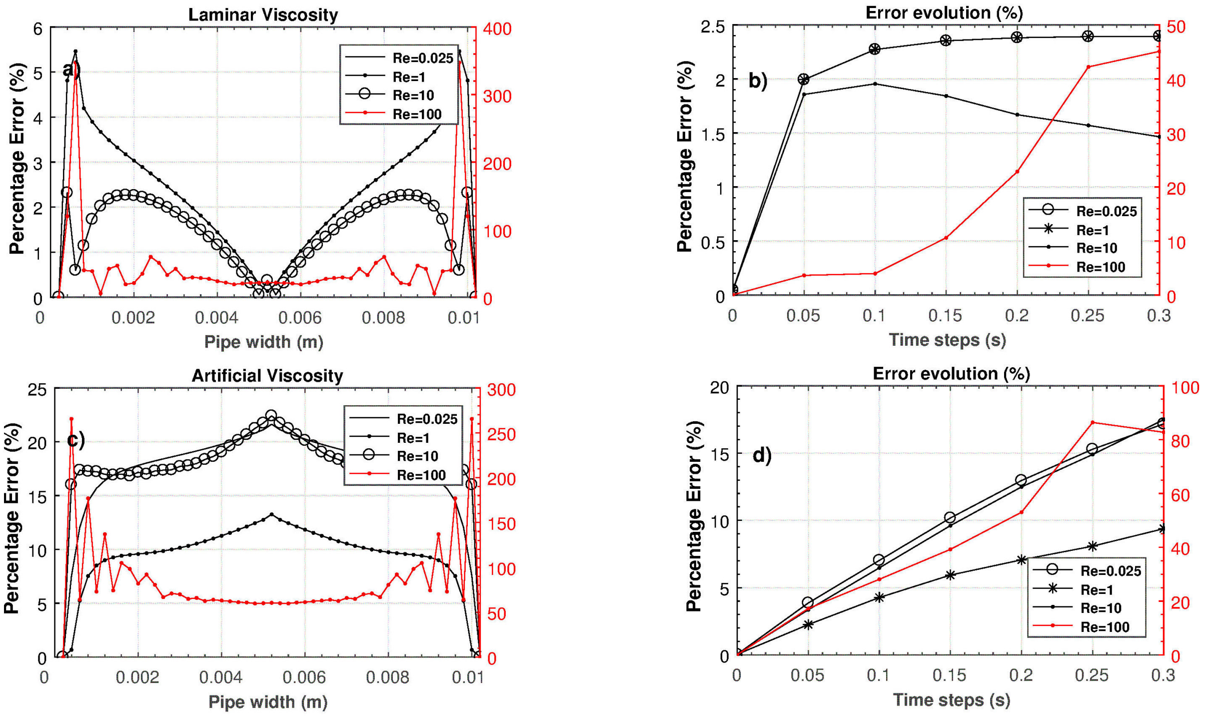

FIGURE 7. Percent error in the full section of the pipe and its time evolution up to 0.3 s for varied Reynolds numbers when working with the laminar (top figures) and the artificial viscosity (bottom figure).

by setting 1500 ghost particles which were uniformly distributed in three layers on each side of the pipe walls. The initial smoothing length was set equal to $h_0 = 1.8ds = 3.6 \times 10^{-5}$ m.

The results of the simulations are displayed in Figs. 7 and 8. Figures 7a) and 7b) display the percent error across the entire pipe section and its time evolution, respectively, for the simulations using the laminar viscosity, while Figs. 7c) and d shows the same when working with the artificial viscosity. In both cases the black curves correspond to Re $= 0.025$, 1, and 10, while the red curve in each plot correspond to the case when Re $= 100$. For all Re-values the maximum errors always occur near the pipe wall when working with the laminar viscosity. These maximum errors are about 5.46% for Re $= 0.025$ and 1, 2.3% for Re $= 10$, and 350% for Re $= 100$. When the laminar viscosity is replaced with the artificial viscosity, the error at the center of the pipe increases to approximately 21.63% when $Re = 0.025$, 13.26% when Re $= 1$, 22.40% when Re $= 10$, and finally, to 265.50% when Re $= 100$. In this latter case, however, the maximum error occurs close to pipe wall and not in the center of the pipe as for Re ≤ 10.

Figures 7b) and d display the time evolution of the velocity errors for the laminar and artificial viscosity, respectively. For Re ≤ 10 the error grows steeply during the first 0.05 s and then at a much slower rate until percent errors less than about 2.5% are achieved by the end of the simulations when a laminar viscosity is used. When Re is increased to 100, the errors grows steadily towards a much higher percent level. When the artificial viscosity is employed the errors all grow steadily to much higher percent values compared to the laminar case. These trends clearly imply that the use of the artificial viscosity introduces much larger average errors in the simulations and therefore it must be used in current flow applications with caution.

Figure 8 depicts the zeroth- and first-order moments of the kernel and its gradient as a function of time, as in the previous cases. The top frames correspond to runs with a laminar viscosity and varying Re, while the bottom frames correspond to identical models using the artificial viscosity. In both cases C^0-particle consistency is approximately achieved almost independently of the Reynolds number. Even when Re $= 100$, the zeroth-order moment of the kernel follows a ragged behavior with values in the worst case ≤ 1.0006 [Fig. 8a)]. A similar behavior is seen in Fig. 8e) when working with the artificial viscosity, with maximum deviations from unity being ≤ 1.0004 in this case. A close inspection of Figs. 8b) and 8f) shows that C^1-particle consistency for the kernel is achieved for Re ≤ 10 when using the laminar viscosity. Again, the worst case occurs for Re $= 100$, where the first-order moment of the kernel oscillates erratically around zero. Since the mean value of the oscillations is close to zero, C^1-particle consistency is also approximately achieved at this high Re. In contrast, when using the artificial viscosity C^1-particle consistency is restored only for Re $= 0.025$, while it is evidently lost for higher values of Re.

The evolution of the zeroth- and first-order moments of the gradient are depicted in Fig. 8c), 8g) and 8d), 8h) for the laminar and artificial viscosity cases, respectively. From Figs. 8c) and d is clear that C^1-particle consistency for the

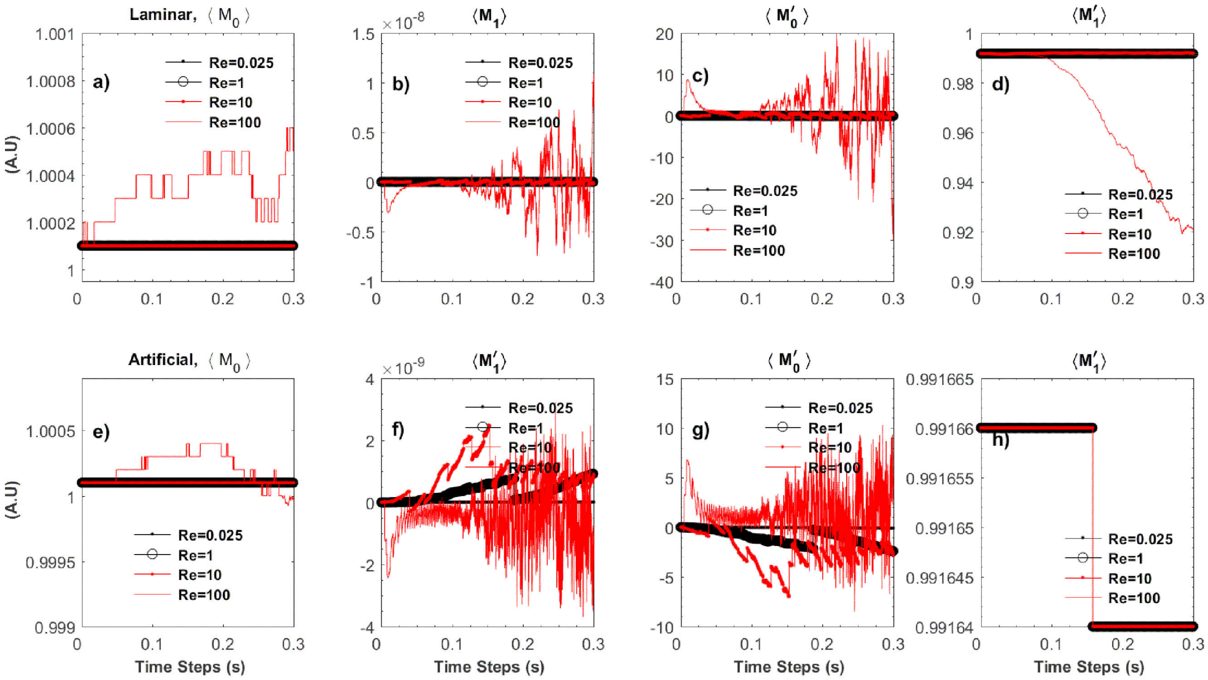

FIGURE 8. Figures a), e) and b), f) show the zeroth- and first-order moments of the kernel, respectively, while figures c), g) and d), h) show the zeroth- and first-order moments of the gradient as a function of time for Poiseuille flow up to 0.3 s for varied Re when working with the laminar (top figures) and the artificial viscosity (bottom figures).

TABLE III. Maximum percent errors and maximum spread values of the zeroth- and first-order moments of the kernel and its gradient for Poiseuille flow at varying Reynolds numbers using a laminar and artificial viscosity in the momentum equation. Letters B and C in the Laminar and Artificial columns refer to the locations of the maximum error: $B \rightarrow Boundaries$, and $C \rightarrow Center$ of the pipe.

	Error Max (%)		First moments of the kernel (a.u)				First moments of the gradient (a.u)			
	Laminar	Artificial	Laminar		Artificial		Laminar		Artificial	
			$\langle M_0 \rangle$	$\langle \mathbf{M_1} \rangle$	$\langle M_0 \rangle$	$\langle \mathbf{M_1} \rangle$	$\langle \mathbf{M'_0} \rangle$	$\langle \mathbf{M'_1} \rangle$	$\langle \mathbf{M'_0} \rangle$	$\langle \mathbf{M'_1} \rangle$
$\mathrm{Re} = 0.025$	B 5.46	C 21.63	1.0001	3.20×10^{-12}	1.0001	7.53×10^{-12}	-0.0716	0.9917	-0.0905	0.9916
$\mathrm{Re} = 1$	B 5.46	C 13.26	1.0001	3.20×10^{-12}	1.0001	9.19×10^{-10}	-0.071	0.9916	-2.4058	0.9913
$\mathrm{Re} = 10$	B 2.31	B 22.40	1.0001	-3.80×10^{-10}	1.0001	2.49×10^{-9}	-0.7557	0.9914	-6.99	0.9893
$\mathrm{Re} = 100$	B 47.39	B 265.50	1.0006	1.08×10^{-8}	1.0004	-3.69×10^{-9}	-30.13	0.9190	10.33	0.9638

gradient is achieved for $\mathrm{Re} \leq 10$ with a very good approximation. However, when Re is raised to 100, the zeroth-order moment is seen to oscillate erratically about zero, while the first-order moment deviates significantly from unity. Thus, at such high value of Re, C^1-particle consistency of the gradient is lost. In contrast, when working with the artificial viscosity, C^1-particle consistency is guaranteed only for $\mathrm{Re} = 0.025$, even though the first-order moment seems to be well-behaved and close to unity for all Re-values. The maximum errors and the maximum values of the first two moments of the kernel and its gradient are listed in Table III for both viscosity formulations and varying Re. Evidently, the maximum errors in both formulations occur for $\mathrm{Re} = 100$, with the artificial viscosity exhibiting larger errors compared to the laminar viscosity at all values of Re. C^1-particle consistency for the kernel is achieved for both viscosity formulations independently of Re, while approximate C^1-particle consistency for the gradient is lost when $\mathrm{Re} = 100$ for the laminar case and when $\mathrm{Re} \geq 1$ for the artificial viscosity.

5. Conclusions

In this work we have explored the effects of the using two different kernel interpolation functions (i.e., a Gaussian kernel versus a Wendland function), varying the scaling of the reference pressure in an equation of state which is typically used in SPH applications of weakly compressible flows, and varying the viscosity formulation from an artificial to a laminar one on the convergence properties of SPH. Here convergence was measured in terms of how accurately the consistency relations for the first two moments of the kernel and gradient are reproduced, which provides information of the order of consistency. As a benchmark test case for this study we have used the simple case of Poiseuille flow in two-space dimensions. This simulation presents validated results upon which the changes are introduced.

The results show that the Wendland function performs in general much better than the Gaussian kernel drastically reducing the errors and improving the consistency. When changing the scaling of the reference pressure in the equation of state, the best results were obtained when the sound speed value, calculated as $c_0 = \delta_c v_{\max}$, was defined with $\delta_c = 0.1$. On the other hand, the use of a laminar viscosity formulation resulted in more accurate results compared to the artificial viscosity.

The results also show that the simulations are sensitive to the value of the Reynolds number (Re) in the sense that, regardless of the method employed, the convergence worsens as Re is increased. This is possibly attributed to the interaction between the fluid and the ghost particles employed to design the pipe wall boundary. As the velocity difference between the stationary ghost particles and the moving fluid ones becomes excessively large, the numerical solution becomes correspondingly less accurate. Although the test case employed here is a simple one, the present results apply to more complex pipe geometries. Future work in this line will extend the present study to three-space dimensions and investigate how the dimensionality may affect the convergence properties of SPH, the initial particle distribution homogeneity and the effect of ghost particles.

Acknowledgments

We acknowledge funding from the European Union's Horizon 2020 Programme under the ENERXICO Project, grant agreement No. 828947 and from the Mexican CONACYT-SENER-Hidrocarburos Programme under Grant Agreement B-S-69926.

Financial disclosure

None reported.

Conflict of interest

The authors declare no potential conflict of interests.

---

1. L. B. Lucy, A numerical approach to the testing of the fission hypothesis. *The Astronomical Journal* **82** (1977) 1013, `https://doi.org/10.1086/112164`.
2. R. Gingold, J. Monaghan, Smoothed particle hydrodynamics theory and application to non-spherical stars. *Monthly Notices of the Royal Astronomical Society* **181** (1977) 375, `https://doi.org/10.1093/mnras/181.3.375`.
3. D.d. Padova, L. Calvo, P. Carbone, D. Maraglino, M. Mossa, Comparison between the Lagrangian and Eulerian Approach for Simulating Regular and Solitary Waves Propagation, Breaking and Run- Up. *Applied Sciences* **11** (2021) 1, doi: `https://doi.org/10.3390/app11209421`.
4. C. Alvarado-Rodríguez, L. Díaz-Damacillo, E. Plaza, L. Sigalotti, Smoothed Particle Hydrodynamics Simulations of Porous Medium Flow Using Ergun's Fixed- Bed Equation. *Water* **15** (2023) 1, doi: `https://doi.org/10.3390/w15132358`.
5. R. Burden, D. Faires, Numerical Analysus. USA: BROOKS COLE. 2010. ISBN 13: 978-0-538-73351-9.
6. C. A. Dutra-Filho, Smoothed Particle Hydrodynamics. *Fundamentals and Basic Applications in Continuum Mechanicsd.* Springer Cham. (2019)
7. F. Rasio, Particle Methods in Astrophysical Fluid Dynamics. *Progress of Theoretical Physics Supplement* **138** (2000) 609, `https://doi.org/10.1143/PTPS.138.609`.
8. R. Gabbasov, L. Sigalotti, F. Cruz, J. Klapp, and J. Ramirez-Velasquez, Consistent SPH Simulations of Protostellar Collapse and Fragmentation. *The Astrophysical Journal* **835** (2017) 25, `https://doi.org/10.3847/1538-4357/aa5655`.
9. J. Read, T. Hayfield, O. Agertz, Resolving mixing in smoothed particle hydrodynamics. *Monthly Notices of the Royal Astronomical Society* **405** (2010) 1513, `https://doi.org/10.1111/j.1365-2966.2010.16577.x`.
10. Q. Zhu, L. Hernquist, and Y. Li Numerical convergence in smoothed particle hydrodynamics. *The Astrophysical Journal* **800** (2015) 6, `https://doi.org/10.1088/0004-637X/800/1/6`.
11. L. Sigalotti, J. Klapp, O. Rendón, C. Vargas, F. Peña-Polo, On the kernel and particle consistency in smoothed particle hydrodynamics. *Applied Numerical Mathematics* **108** (2016) 242, `https://doi.org/10.1016/j.apnum.2016.05.007`.
12. L. Sigalotti O. Rendón J. Klapp C. Vargas and F. Cruz, A new insight into the consistency of the SPH interpolation formula. *Applied Mathematics and Computation* **356** (2019) 50, `https://doi.org/10.1016/j.amc.2019.03.018`.
13. D. Violeau and T. Fonty, Calculating the smoothing error in SPH. *Computers and Fluids* **191** (2019) 104240, `https://doi.org/10.1016/j.compfluid.2019.104240`.
14. L. Landau, and E. Lifshitz Fluid Mechanics. (Oxford: Pergamon Press. 1987). ISBN 0-08-033933-6.
15. J. Klapp, Sigalotti LDG, Alvarado-Rodríguez CE, Rendón O, Díaz-Damacillo L. Approximately consistent SPH simulations of the anisotropic dispersion of a contaminant plume. *Computational Particle Mechanics* **9** (2022) 987, `https://doi.org/10.1007/s40571-022-00461-1`.
16. G. Batchelor, An Introduction to Fluid Dynamics. Cambridge: (Cambridge University Press. 1967).

17. J. Morris, P. Fox, and Y. Zhu, Modeling Low Reynolds Number Incompressible Flows Using SPH. *Journal of computational physics* **136** (1997) 214, https://doi.org/10.1006/jcph.1997.5776.
18. A. Tartakovsky *et al*., Smoothed particle hydrodynamics and its applications for multiphase flow and reactive transport in porous media. *Computational Geoscience* **20** (2015) 807, https://doi.org/10.1007/s10596-015-9468-9.
19. J. Monaghan, Smoothed particle hydrodynamics. *Reports on Progress in Physics* **68** (2005) 1703, https://doi.org/10.1088/0034-4885/68/8/R01.
20. A. Colagrossi, and M. Landrini, Numerical simulation of interfacial flows by smoothedparticle hydrodynamics. *Journal of computational physics* **191** (2003) 448, https://doi.org/10.1016/S0021-9991(03)00324-3.
21. J. Monaghan and R. Gingold, Shock Simulation by the Particle Method SPH. *Journal of Computational Physics* **52** (1983) 374, https://doi.org/10.org/10.1016/0021-9991(83)90036-0.
22. E. Lo, and S. Shao, Simulation of near-shore solitary wave mechanics by an incompressible SPH method. *Applied Ocean Research* **24** (2002) 275, https://doi.org/10.1016/S0141-1187(03)00002-6.
23. G. Liu, M. Liu, Smoothed Particle Hydrodynamics: A Meshfree Particle Method. Singapore: (World Scientific. 2003).
24. J. Monaghan, Smoothed particle hydrodynamics. Annual *Review of Astronomy and Astrophysics* **30** (1992) 543, https://doi.org/10.1146/annurev.aa.30.090192.002551.
25. D. Price, Smoothed particle hydrodynamics and magnetohydrodynamics. *Journal of Computational Physics* **231** (2012) 759, https://doi.org/10.1016/j.jcp.2010.12.011.
26. S. Nugent and H. Posch Liquid drops and surface tension with smoothed particle applied mechanics. *Physical Review E* **62** (2000) 4968, https://doi.org/10.1103/Phys-RevE.62.4968.
27. L. Sigalotti, J. Klapp, E. Sira, Y. Meleán, and A. Hasmy, SPH simulations of time-dependent Poiseuille flow at low Reynolds numbers. *Journal of Computational Physics* **191** (2003) 622, https://doi.org/10.1016/S0021-9991(03)00343-7.
28. Y. Meleán, L. Sigalotti, and A. Hasmy, On the SPH tensile instability in forming viscous liquid drops. *Computer Physics Communications* **157** (2004) 191, https://doi.org/10.1016/j.comphy.2003.11.002.
29. F. Jiang M. Oliveira, and A. Sousa, Mesoscale SPH modeling of fluid flow in isotropic porous media. *Computer Physics Communications* **176** (2007) 471, https://doi.org/10.1016/j.cpc.2006.12.003.
30. P. Kunz *et al*., Study of multi-phase flow in porous media: Comparison of SPH simulations with micro-model experiments. *Transport in Porous Media* **114** (2015) 581, https://doi.org/10.1007/s11242-015-0599-1.
31. R. Canelas, A. Crespo, J. Dominguez, R. Ferreira, and M. Gomez- Gesteira, SPH-DCDEM model for arbitrary geometries in free surface solid-fluid flows. *Computer Physics Communications* **202** (2016) 131, https://doi.org/10.1016/j.cpc.2016.01.006.
32. E. Plaza *et al*., Efficiency of particle search methods in smoothed particle hydrodynamics: a comparative study (part I). *Progress in Computational Fluid Dynamics* **21** (2021) 1, https://doi.org/10.1504/PCFD.2021.112625.
33. W. Dehnen and H. Aly, Improving convergence in smoothed particle hydrodynamics simulations without pairing instability. *Monthly Notices of the Royal Astronomical Society*, **425** (2012) 1068, https://doi.org/10.1111/j.1365-2966.2012.21439.x.
34. H. Wendland, Piecewise polynomial, positive definite and compactly supported radial functions of minimal degree. *Advances in Computational Mathematics* **4** (1995) 389, https://doi.org/10.1007/BF02123482.
35. K. Urbanowicz, A. Bergant, M. Stosiak, A. Deptuła, M. Karpenko, Navier-Stokes Solutions for Accelerating Pipe Flow - A Review of Analytical Models. *Energies*, **16** (2023) 1, https://doi.org/10.3390/en16031407.
36. A. Chorin, A numerical method for solving incompressible viscous flow problems. *Journal of Computational Physics*, **2** (1967) 12, https://doi.org/10.1016/0021-9991(67)90037-X.
37. C. Alvarado-Rodríguez, J. Klapp, L. Sigalotti, J. Domínguez, d. lE. Cruz-Sánchez, Nonreflecting outlet boundary conditions for incompressible flows using SPH. *Computers and Fluids* **159** (2017) 177, https://doi.org/10.1016/j.compfluid.2017.09.020.
38. J. Monaghan, J. Lanttazio, A refined particle method for astrophysical problems. *Astronomy and astrophysics* **149** (1985) 135,
39. L. Libersky, A. Petschek, T. Carney, J. Hipp, and F. Allahdadi High Strain Lagrangian Hydrodynamics: A Three- Dimensional SPH Code for Dynamic Material Response. *Advances in Computational Mathematics*, **109** (1993) 67, https://doi.org/10.1006/jcph.1993.1199.
40. J. Monaghan, Simulating free surface flows with SPH. *Journal of Computational Physics*, **110** (1994) 399, https://doi.org/10.1006/jcph.1994.1034.
41. S. Liu, I. Nistor, M. Mohammadian, Evaluation of the Solid Boundary Treatment Methods in SPH. *International Journal of Ocean and Coastal Engineering* **1** (2018) 1, https://doi.org/10.1142/S252980701840002X.
42. P. Randles, L. Libersky, SPH Modeling of Solid Boundaries Through a SemiAnalytic Approach. *Computer Methods in Applied Mechanics and Engineering* **139** (1996) 375, https://doi.org/10.1016/S0045-7825(96)01090-0.
43. A. Monaco, S. Manenti, M. Gallati,and S. Sibilla, Agate G, Guandalini R. SPH Modeling of Solid Boundaries Through a SemiAnalytic Approach. *Engineering Applications of Computational Fluid Mechanics* **5** (2011) 1, https://doi.org/10.1080/19942060.2011.11015348.
44. H. Takeda, S. Miyama, M. Sekiya, Numerical Simulation of Viscous Flow by Smoothed Particle Hydrodynamics. *Progress of Theoretical Physics* **92** (1994) 939, https://doi.org/10.1143/ptp/92.5.939.

45. G. Johnson, and S. Beissel, Normalized smoothing functions for SPH impact computations. *International Journal for Numerical Methods in Engineering* **39** (1996) 2275,
46. I. Schoenberg, Contributions to the Problem of Approximation of Equidistant Data by Analytic Functions. In: de Boor C. I. J. *Schoenberg Selected Papers* **4** (1946) 3, `https://doi.org/10.1007/978-1-4899-0433-1-1`.
47. J. Morris and J. Monaghan A switch to reduce SPH viscosity. *Journal of computational physics* **136** (1997) 41, `https://doi.org/10.1006/jcph.1997.5690`.